ARTICLE

Ultramicroporous Carbon Aerogel Encapsulating Sulfur as Cathode for Lithium-Sulfur Batteries

Received 00th January 20xx,
Accepted 00th January 20xx

DOI: 10.1039/x0xx00000x

Maryam Nojabaee[*, a], Brigitta Sievert[a], Marina Schwan[b], Jessica Schettler[b], Frieder Warth[a], Norbert Wagner[a], Barbara Milow[b, c], K. Andreas Friedrich[a,d]

Abstract

Highly porous carbon materials employed in sulfur cathodes are of utmost importance to charge transport, conductivity and stability of cathode in metal-sulfur batteries. Herein, ultra-microporous carbon aerogels as conductive matrix embedding sulfur for cathode application in lithium-sulfur batteries are synthesized and investigated. Resulting from organic resorcinol-formaldehyde aerogels, the synthesized carbon aerogels feature a highly porous structure with the surface area of 500-2000 $m^2 g^{-1}$ and large micropore volume up to 0.6 $cm^3 g^{-1}$. The effective gas-phase sulfur infiltration of the carbon aerogels and the resulting confinement of sulfur in the micropores are demonstrated. It is indicated that sulfur-infiltrated microporous carbon aerogel cathodes are able to suppress the polysulfide shuttle effect, maintaining 80% (≥1000 Ah $kg_{(S)}^{-1}$) and 70% (≥800 Ah $kg_{(S)}^{-1}$) of initial discharge capacity after 200 cycles at the rate of 0.3C in carbonate and ether-based electrolyte, respectively. Remarkably, herein prepared composite cathode can still deliver a discharge capacity of at least 700 Ah $kg_{(S)}^{-1}$ at faster rate of 2C in both electrolyte systems. The cyclability and compatibility of the ether and carbonate-based electrolyte with such composite cathode are discussed elaborately.

Introduction

Electrochemical storage devices such as lithium-based battery systems are of great essence for several key applications including electrification of transport and stationary storage of renewable energy. In regard to these applications, high energy densities in addition to durability, safety and temperature tolerance are decisive prerequisites.[1] Potential alternatives for the realization of these applications are chemistries beyond lithium-ion batteries such as lithium-sulfur (Li-S) systems. Sulfur (S) as the active species in the positive electrode enables a theoretical gravimetrical capacity of 1675 Ah kg^{-1} and energy density of 2600 Wh kg^{-1} (with respect to S mass and in combination with lithium (Li) metal) through the conversion reaction and formation of Li_2S.[2, 3] Li-S batteries, which in recent years have been targeted for a high gravimetric energy density of 400-500 Wh kg^{-1}, show a particular potential not only in the aerospace applications such as aviation, high altitude pseudo-satellite (HAPS) and drones but also heavy-transport.[4, 5]

However, commercially aimed Li-S batteries are still hampered by various challenges, such as low S utilization, enormous volume expansion, polysulfide shuttle effect and Li dendrite formation.[6, 7] The poor conductivity of S and its corresponding discharge products demand a conductive component facilitating electron transfer and thereby the charge transfer to suppress the sluggish redox kinetics. Additionally, the

[a.] German Aerospace Center (DLR), Institute of Engineering Thermodynamics, Stuttgart, Germany Address here.
[b.] German Aerospace Center (DLR), Institute of Material Research, Cologne, Germany
[c.] University of Cologne, Institute of Inorganic Chemistry, Cologne, Germany
[d.] University of Stuttgart, Institute for Building Energetics, Stuttgart, Germany
† Autor 1 and autor2 contributed equally.
Electronic Supplementary Information (ESI) available: [details of any supplementary information available should be included here] See DOI: 10.1039/x0xx00000x

conversion reaction of S and the formation of Li_2S cause a substantial volume expansion (≈ 80%), which disintegrates the ionic and electronic percolation pathways, resulting in the suppression of kinetic rates.[8] To address these issues, the optimization of the S cathode was pursued using various strategies.[9-12] Among the most commonly employed is the embedding of S in a porous carbon material providing high electronic conductivity along with the ability to trap the S to effectively cushion the volume changes during S lithiation and delithiation. To this end, carbon materials ranging from graphene, reduced graphene oxide (rGO), carbon nanotubes, carbon nanofibers and porous carbons with different pore characteristic have been investigated.[13-18] Commercially available types of carbon black with high specific surface area do not always possess sufficient share of pore volume with the desirable size.[19] Microporous carbon materials in particular exhibit a promising performance, explained by the capture and confinement of the S in the micropores.[20, 21] Hereby the structure and volume of the porosity as well as the S infiltration process are of great importance to achieve high S utilization and stable performance in microporous carbon. Despite the disadvantage of the S-loading being limited, such an approach offers the possibility of using carbonate-based electrolytes. The excessive nucleophilic reaction of the carbonate solvent with the short-chain S anions needs to be hindered, whether by chemically bound or physically entrapped S in micropores less than 2 nm.[22, 23] The physical confinement of S in ultramicropores prevents direct contact between S and liquid electrolyte, resulting in a quasi-solid-state reaction between S and lithium and a direct conversion of S to lower order polysulfide.

There have been multiple approaches in the literature including melt, solution and gas-based infiltration methods to encapsulate S into carbon materials suppressing the formation of the solvated polysulfide and redox shuttle.[16, 24-27] With regard to the S infiltration procedure of microporous carbons, a proven technique as opposed to the state-of-art melt infiltration is the gas phase infiltration at lower pressures for solid-state and polysulfide-free conversion reaction of lithium sulfide in Li-S batteries.[28]

Carbon aerogels (CA) as open-porous solid materials offer a high freedom of material design to adapt the host structure to the requirements of an electronically conductive, S species retaining electrode matrix.[29] Aerogels are usually synthesized in a sol-gel process followed by various drying methods. During synthesis, drying and carbonization, the properties and the microstructure can be adjusted for the intended application, e.g. generation of different pore sizes, wide or narrow pore size distribution.[30] Therefore, the particular importance of aerogels resides in the adaptable and reproducible morphology. Aerogels can be varied concerning electrical conductivity, mechanical flexibility, micropore/mesopore ratio and content offering low density, cost efficient production and therefore large-scale applications for electrode materials or foundries. In fact, only few studies report on the use of CA as S host so far and moreover the importance of micropore confinement was not considered.[31, 32]

Herein, a novel and highly microporous CA material is synthesized and its applicability for S cathodes is evaluated. For this purpose, a S-vapor infiltration process is investigated and qualified, in which the synthesized CAs are used as conductive host material. The new CA-S electrodes are compared to conventional S-C composite electrodes with respect to their performance in both carbonate and ether-based electrolytes. The successful S encapsulation was demonstrated in carbonate-based electrolytes. This is an important leap forward to commercialization, as carbonate-based electrolytes are cheaper and commercially available in battery quality purity and well-studied due to their applications in advanced lithium ion batteries.[33] Additionally, the flexible CAs offering reversible deformation during volume exchange upon charge and discharge allows minimizing the formation of cracks and extending the cycle life of the cell. Besides that, the influence of the microporosity versus the electrolyte nature on the discharge behaviour of such S composite electrodes is discussed in detail to initiate further research in these promising type materials.

Experimental

Synthesis of CAs

The synthesis of flexible CA is an extension of the previous work by Schwan et al.[34] In the first step resorcinol-formaldehyde (RF) aerogels were synthesized. At room temperature, resorcinol (R) (98%, Aldrich) was dissolved in deionized water (W) and stirred at 150 rpm. Subsequently, an aqueous solution of formaldehyde (F) (37% w/w, stabilized with 10% methanol, Merck) and solid sodium carbonate (Cat) (Aldrich) were added to the stirred resorcinol solution. The molar ratios of used chemicals follow as: R/F = 0.5; R/W = 0.008 and R/Cat = 50. After 5 minutes, the pH of RF solution was adjusted to 5.4 - 5.6 via dropwise addition of 2N nitric acid solution (Alfa Aesar). Continued stirring at room temperature, followed by transferring the homogeneous transparent solution in a sealable polypropylene container to an oven at 60°C for seven days. To remove residual reagents and exchange water for acetone which is soluble in supercritical carbon dioxide, the wet gel was cooled to room

temperature after seven days of gel formation and aging and placed in an acetone bath. The acetone washing was repeated six times within three days. The supercritical drying was carried out with CO_2 (purity ≥ 99.995%, Praxair) in an autoclave of 60 L volume (Eurotechnica) at 60°C and 110 bars for about 21 h, with the degassing rate of 0.2 bars per minute. The resulting RF aerogel was carbonized in second step. The aerogel was purged three times with argon (purity ≥ 99.996%, Praxair) prior to carbonization at 1000 °C. The heating up rate was adjusted to 6-7 K min^{-1}, and argon was passed through the furnace applying a pressure of 4 bars. This sample was named CA(Ar). An additional sample labeled CA(N_2/CO_2) was carbonized under nitrogen atmosphere (purity ≥ 99.999, Linde, Germany) at 800 °C for 5h, followed by 3h activation with CO_2 at 1000 °C. The flow rate of both N_2 and CO_2 was adjusted to 22 L h^{-1}, the heat rate to 5 K min^{-1}. After carbonization, aerogels were cooled down to room temperature under a flow of nitrogen.

S Infiltration and Cathode Preparation

Infiltration of elemental S inside the pore space of the CA and a selective evaporation of the remaining S from the carbon surface was performed in a two-step procedure. Firstly, CA and sublimed S (99.5 %, Alfa Aesar) with the ratio of CA:S is 44:56 were mixed and grinded using the ball mill (Pulverisette 7, Fritsch). Secondly, the obtained CA+S powder was sealed in a glass ampule under argon atmosphere. The mixture was heated at 600°C for 6 h with heating rate of 5 K min^{-1}. At this high temperature the S evaporates and diffuses into the pores obtaining the CA+$S_{inf,St1}$ powder.[12,23] In a third step, to eliminate the S residues on the surface of the carbon, the mixture was heated in a glass tube with condensation trap to 300°C for 90 minutes. The so prepared (CA+S_{inf}) powder was mixed with water-based binders CMC (Walocel CRT 2000 PA, Dow) and PEO (Sigma Aldrich, average M_v 600,000) in a ratio of 90:3:7 and the obtained slurry was coated onto aluminum foil using doctor blade method. Electrodes were punched out with a diameter of 18 mm and a S-loading of 0.8 mg_S cm^{-2} for electrochemical characterization. Cells with S electrodes in a corresponding loading made from commercially available Ketjenblack (KB) and CA mechanically mixed with S were prepared for comparison.

Cell Assembly and Electrochemical Measurements

For the electrochemical measurements, batteries were assembled under argon atmosphere in using EL Cell®. A 0.75 mm thick lithium anode (99.9 %, Sigma Aldrich) (diameter of 18 mm) with a diameter of 18 mm was electrically separated from the cathode via a 25 µm thick polypropylene membrane (Celgard 2500). The performance of two electrolytes with electrolyte:S (E:S) ratio of 40 µL electrolyte per mg S was investigated: (i) 1M lithium bis(trifluoromethylsulfonyl)imide (LiTFSI) in 1.3-dioxolane / dimethoxy ethane (DOL/DME, 1:1), (ii) 1M $LiPF_6$ in ethylene carbonate / diethylene carbonate (EC:DEC 50:50 vol%, Sigma Aldrich). For the electrode with higher loading the electrolyte amount was adjusted to the 20 µL mg^{-1}. A typical discharge-charge cycling test was carried out, after 12 h open-circuit-voltage (OCV), with a formation phase of 167.5 A kg^{-1} (0.1C) followed by the actual cycling phase with 558.4 A kg^{-1} (0.3C) in the voltage range of 1V to 3.3 V. Electrochemical impedance spectroscopy (EIS) was performed in a symmetrical CA(Ar)+S_{inf} cathode in the EL Cell® setup using an electrochemical workstation (Zahner® IM6 with Thales battery software). The EIS was carried out with an excitation voltage of 10 mV in a frequency range of 5MHz and 50 mHz.

Characterization

The bulk density of CA was calculated from measured volume and weight of an aerogel piece. The skeletal density was measured with AccuPyc 1360 (Micromeritics, USA). Surface area, pore volume and mesopore size distribution of aerogels and aerogels infiltrated with S were determined by nitrogen adsorption-desorption using BET and BJH methods (77 K), additionally with help of t-plot method the micropore volume and micropore surface area were determined. The micropore size distribution was obtained by carbon dioxide adsorption (273 K) using density functional theory (DFT) (TriStar II, Micromeritics, USA). Before analysis, the CAs were outgassed for 24 h at 200°C and 0.1 mbar, samples infiltrated with S were outgassed for 24 h at 40°C and 0.1 mbar. The electrical conductivity was measured with four-point electrodes based on a DC voltage-current measurement (Loresta, Mitsubishi Chemical Europe) under different pressures by using a powder resistivity measurement system (PD-51, Mitsubishi Chemical Europe). Approx. 1g of the sample was added into a cylindrical form and compacted with defined pressure. The thickness of the sample is determined using a displacement transducer. A STA 449C Jupiter® (Netzsch) was used for thermal gravimetrical analysis (TGA) to determine the S content and analyze the S infiltration. The samples were heated to 1200 °C with 5 K min^{-1} in an Al_2O_3 crucible under argon atmosphere. X-ray diffractograms were recorded using an x-ray diffractometer (D8 Discover Bruker GADDS) with a VÅNTEC-2000 detector. The spectra were taken on reflection mode using a tuned monochromatic and parallel x-ray beam (Cu-Kα). The accelerating voltage and the tube current were 45 kV and 0.650 mA, respectively. The XPS measurements were performed on a VersaProbe II System by Ulvac-Phi using monochrmatic Al Kα light with a photon energy of 1486.6 eV.The surface morphology and microstructure

of the coated electrodes before and after cycling were characterized by scanning electron microscopy (SEM, Zeiss ULTRA plus).

Result and discussion

CA Synthesis and CA+S_{inf} Cathode Preparation

As demonstrated in Figure 1 , the overall cathode preparation of CA+S_{inf} involves a sol-gel synthesis of the resorcinol-formaldehyde aerogel and the follow-up carbonization to the CA as well as two-steps gas phase infiltration of the S into the micropores of the CA.[35] Derived from organic resorcinol-formaldehyde, the aerogels provide highly porous structure with porosity up to 97%, high surface area about 500-2000 $m^2\ g^{-1}$, large micropore volume of 0.1-0.6 $cm^3\ g^{-1}$, and high electronic conductivity of 80-150 $S\ m^{-1}$. The microstructure can be adjusted upon synthesis and carbonization of organic aerogels. The herein synthesized CAs offer high flexibility and could be reversibly deformed up to 30% owing to its interconnected pore microstructure.[34]

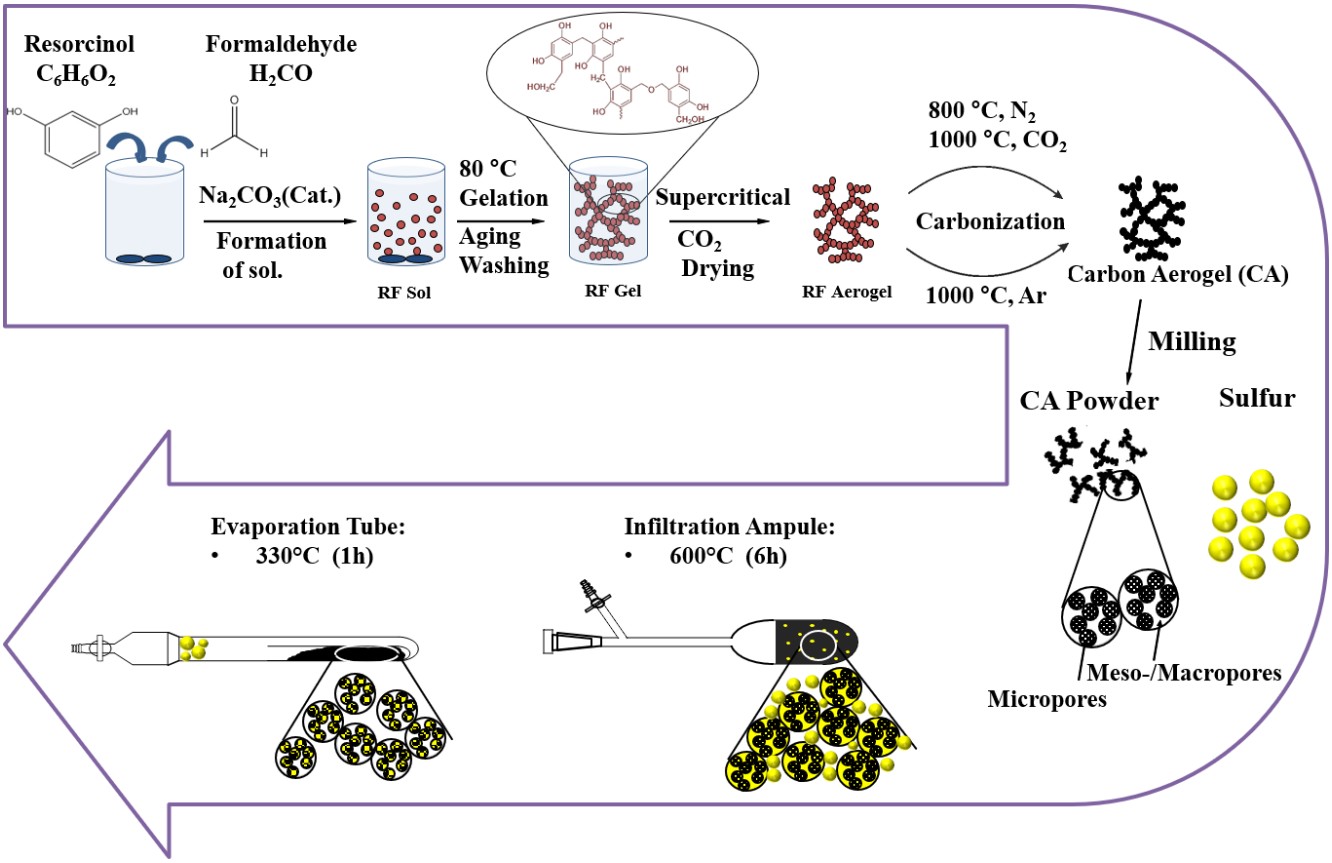

Figure 1 Schematic of CA synthesis and the developed gas-infiltration method.[35]

In the presented work, the flexible resorcinol-formaldehyde aerogels are subjected to the carbonization by two distinct formulations, i.e. utlizing either Ar or N_2/CO_2 upon carbonization process. The main objective of activation with CO_2 is to develop a high microporosity in the aerogel network.[36]

The properties of developed CAs are summarized in Table 1:

Table 1: Properties of CAs with CA(Ar)and without activation CA (N_2/CO_2).

Properties	CA(Ar)	CA(N_2/CO_2)
Skeletal density [g/cm³]	2.72	2.71
Bulk density [g/cm³]	0.04	0.07
Porosity [%]	98.6	97.3
Specific surface area [m²/g]	561	1912
Micropore volume [cm³/g]	0.18	0.60
Mesopore volume [cm³/g]	0.04	0.28
Particle size [µm]	0.1	0.09

While both aerogels exhibit high porosity of about 97-98 %, the CA(N_2/CO_2) sample shows higher bulk density due to the longer carbonization time. The specific surface area and pore volumes vary considerably. The activated CA(N_2/CO_2) has almost four times higher specific surface area. Figure 2a depicts the isotherms for both samples. The isotherm of CA(Ar) may be considered as type I according to IUPAC and the isotherm of CA(N_2/CO_2) is an intermediate between type I and IV with a noticeable amount of adsorbed nitrogen at low and high relative pressures. The pore volume is increased likewise during N_2/CO_2 carbonization. This total increase in pore volume is due to a combination of releasing volatiles and oxidation of char with carbon dioxide. The endothermic Boudouard reaction between carbon and carbon dioxide takes place rapidly at 1000 °C and the equilibrium is shifted to CO, resulting in both: formation and widening of pores. The pore size distribution is shown in Figure 2b. In the micropore range, the pore sizes of both aerogels are comparable. However, in the mesoporous range the sample CA(N_2/CO_2) differs significantly from CA(Ar), with latter possessing only a small amount of mesopores (0.04 $cm^3 g^{-1}$). The creation of mesopores occurred during long activation time.[37] Both samples have a particle size of about 100 nm, observed in the SEM image in Figure 2c and 2d. Particularly noticeable is the difference in shape of the particles, indicating the formation of angled particle upon activation with CO_2. Furthermore, the Raman spectra, shown in Figure 2e reveal the structural differences between these two aerogels in consistency with the SEM images. The G peak at 1580 cm^{-1} is caused by bond-stretching motion of carbon sp^2 atoms, organized in rings or chains. The D peak is around 1350 cm^{-1} and is originated from the breathing mode of sp^2 carbon organized in six-fold aromatic rings in the presence of defects. The presence of both peaks indicates that CA has structure with graphitic cluster dispersed in disordered carbon. The intensity ratio of I_D/I_G are 0.8 and 1.1 for CA(N_2/CO_2) and CA(Ar), respectively, indicating an emerging disorder and decrease in cluster size. The decrease of I_D and slight increase of I_G for CA(N_2/CO_2) corresponds to the growth of crystallites during partial graphitization owing to the longer carbonization time which results in higher degree of graphitization and more ordered structure with increase of cluster size.[38, 39] The heat treatment plays a crucial role of enhancement in structural ordering, thus higher graphitization level of activated CA(N_2/CO_2). The electrical conductivity of CAs was measured at different contact pressures (Figure S1) with higher conductivity for both samples upon increasing the contact pressure due to the lowered contact resistance. The slight difference in conductivity is due to the difference in the bulk density as well as the degree of graphitization.[40]

ARTICLE

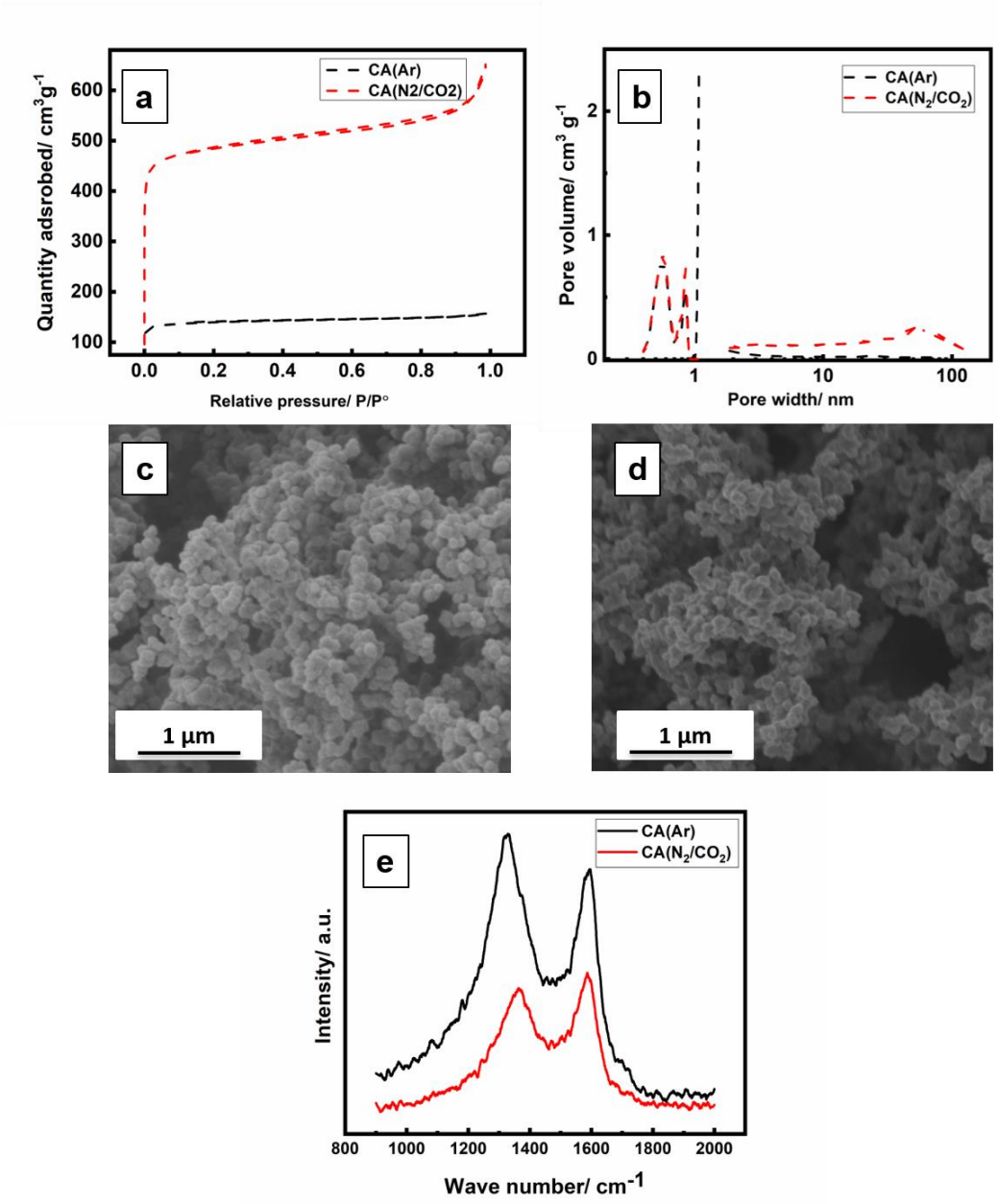

Figure 2(a) N_2-isotherms of CAs at 77 K. (b) Size distribution calculated with BJH (N_2 adsorption at 77 K) and DFT (CO_2 adsorption at 273 K). (c) Microstructure of CA (Ar) and (d) of CA (N_2/CO_2), (e) Raman spectra recorded for CAs in the range at 900-2000 cm^{-1}.

Herein, the two steps infiltration via the gas phase, illustrated schematically in Figure 1, is employed as an effective approach filling up the ultramicropores of the synthesized CA with short-chain S (S_n, n≤6). At room temperature (RT) S is present in the form of S_8 cycle. With increasing temperature at 445°C it transforms into gaseous phase mostly formed of S_8 with the length to be decreased upon raising temperature. At lower pressure and temperatures above 600°C, S_2 is the prevalent form.[41] In this state the short-chain S_2 (≈0.4 nm in diameter) can diffuse and allocate into the micropores. Accordingly, while the micropores are filled with short-

chain S, the existing macrospores and the surface contain the relatively larger remaining S which was selectively removed in the subsequent evaporation step.

Figure 3a-c present SEM images of CA+S composites at three different preparation stages of mechanical mixing (Figure 3a, CA(Ar)+S_{mixed}), the first-step of infiltration (Figure3b, CA(Ar)+$S_{inf(st1)}$) and the second-step of infiltration (Figure3c, CA(Ar)+S_{inf}). Due to the higher atomic weight of S compared to the carbon, S areas are displayed in higher brightness. While in the images of the mixed powder (CA(Ar)+S_{mixed}) and the first infiltration step (CA(Ar)+$S_{inf(St1)}$) the S is still clearly visible, it can be confirmed that the second evaporation step (CA(Ar)+S_{inf}) successfully eliminates the extra surficial S.

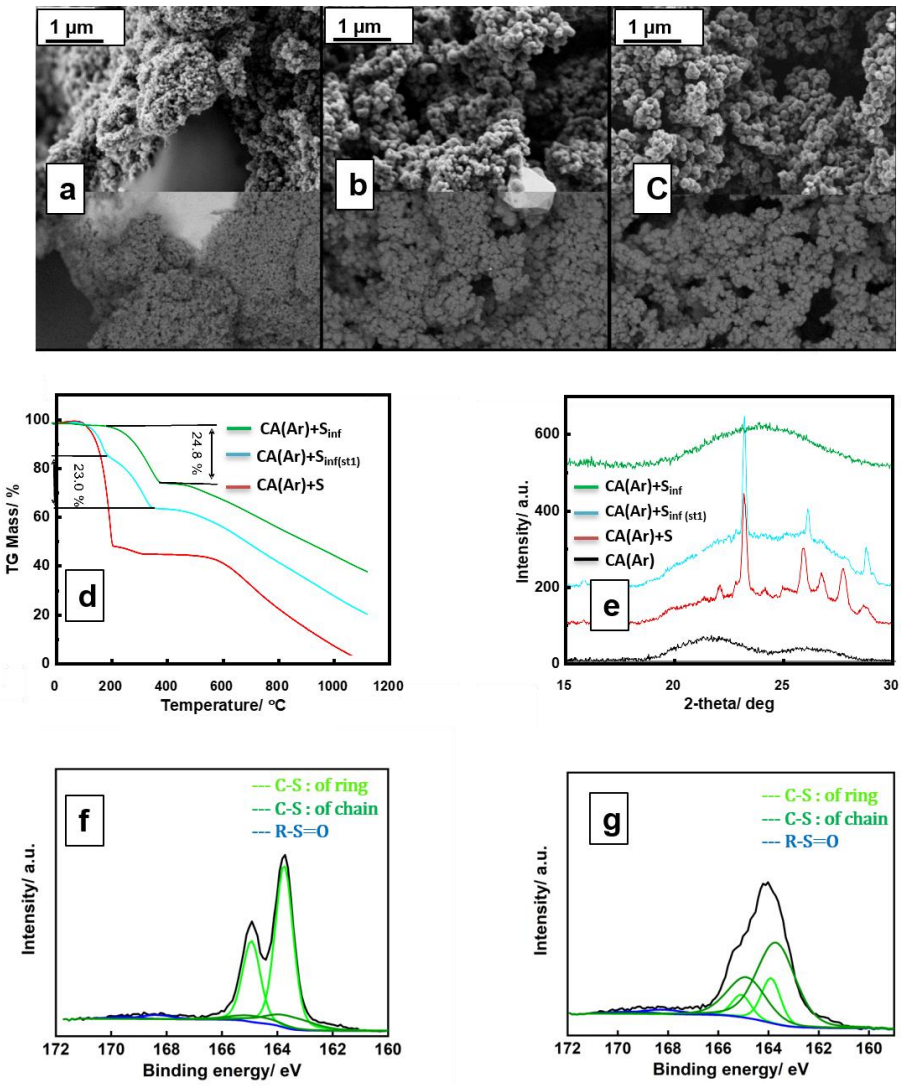

Figure 3 SEM images of (a) CA+ S_{mixed}, (b) CA+$S_{inf,st1}$, (c) CA+S_{inf} composite. (d) TGA measurements of CA and S mixture compared to the S infiltrated composites. (e) XRD pattern of CA (black), CA+ S_{mixed} (red), CA+$S_{inf,st1}$(blue), CA+S_{inf} (green) composite, S 2p signal of the recorded XPS spectra for (f) CA(N_2/CO_2)+S_{inf} (g) CA(Ar)+S_{inf}.

The TGA-measurements shown in Figure 3d indicate that evaporation of S, coordinated to the walls of the pores proceeds at different temperatures than external S deposits. The mixture of S and CA prior to the infiltration process (CA(Ar)+S) comprises two regions. The mass reduction between 180°C and 230°C is ascribed to S evaporation followed by the oxidation of carbon at 500°C. For the TGA measurement of the composite after the gas-infiltration process (CA(Ar)+$S_{inf(st1)}$, blue curve) an additional mass-loss region appears at higher temperatures than the initial evaporation of S with a 23wt.% mass loss. This is assigned to the S trapped inside

the micropores of the aerogels and coordinated to the walls of the pores demanding additional energy for evaporation. Nevertheless, there is still S evaporating at lower temperatures. This S is either located in the mesopores or at the surface in a S_8 state. The aim of the second evaporation step at 300°C is to eliminate this undesired S. TGA analysis performed after this step CA(Ar)+S_{inf} reveals the almost complete elimination of the non-coordinated S indicating the maximum S accommodation of the 24wt.%. This could naturally be further increased to 31wt.% for CA(N_2/CO_2)+S_{inf} sample showing higher microporosity as already discussed (see Figure S2). However, taking into account the N_2- and CO_2-physisorption measurements for the CA(N_2/CO_2)+S_{inf} sample shown in Figure S3, the entire elimination of S from the mesopores in the range of 2-20 nm are not achieved with the evaporation step, meaning that not all the coordinated S are located in micropores. Indeed, the N_2-adsorption measurements have shown that 0.08 cm^3 g^{-1} volume of mesopores in CA(N_2/CO_2) are filled with S after evaporation, see Figure S4. In this pores S can be distributed as S_8 rings and can be lost during first cycles. This points that the developed process is most suitable for the highly microporous carbon material in the absence of mesopores. Presence of even the small portion of the mesopores could be detrimental to the entire confinement of the S in the micropores. This will be discussed more in details in the electrochemical results. The CA(Ar)+S composites after various heat treatment steps as well as the base materials were further analyzed via XRD, shown in Figure 3e. The pattern of the CA(Ar)+S_{mixed} sample before heat treatment shows diffraction peaks according to the crystalline structure of S with an underlying signal of amorphous carbon structures. For the C(Ar)+$S_{inf,st1}$ composite obtained after the gas-infiltration process the intensity of the S related peaks is reduced as substantial amount of S is present in the CA-pores in amorphous form or nano-crystalline. For the CA(Ar)+S_{inf} composite obtained after the second evaporation process, the crystalline peaks have fully vanished. To understand the nature of coordination between S and carbon the X-ray photoelectron spectroscopy (XPS) measurement has been implemented. Figure 3f illustrate the C1s signal of recorded spectra for CA(N_2/CO_2)+S_{inf} sample. Here the presence of S is confirmed by the S 2p signal of CA(Ar)+S_{inf} which is ascribed by the deconvolution of signal into two sets of S 2p3/2 and 2p1/2 doublet with an energy shift of 1.2 eV. Evaluation of the XPS yields an amount of about 15at% of S and minimal amounts of oxygen <2at%, with the remaining concentration attributed to C. The S 2p3/2 peak with the binding energy of 163.8 eV (light green) is assigned to C-S species. The prominent difference between two samples is that CA(N_2/CO_2)+S_{inf} sample shows a clear doublet structure while CA(Ar)+S_{inf} features much broader doublet peaks, see Figure 3g. Hence, the assumption is taken that in CA(N_2/CO_2)+S_{inf}, S is bond to the aromatic ring, whereas in CA(Ar)+S_{inf} there is a mixture of S to ring and S to chain/amorphous carbon. This is supported by C1s peaks, see Figure S4 which is much broader and less sp2 like for the sample with the broad S 2p peak, corroborating the discussions on the structure and graphitization-degree based on the Ramen spectra. The peak at 168.2 eV in figures 3f and g is attributed to the sulfate species formed by S oxidation and makes less than 4% of the total S signal and is hence negligible.[42]

Electrochemical Performance

The electrochemical performance of CA+S_{inf} cathode is evaluated using the El-Cell setup with Li metal as the anode. Figure 4a illustrates the voltage-capacity profile of the so-prepared S-loaded CA electrodes CA(Ar)+S_{inf} in the range of 1-3.3 V in 1M LiPF6:EC/DEC electrolyte. For the purpose of comparison, S cathodes with commercial mesoporous Ketjenblack (KB+S_{mixed}) and CA using the pure mixing method (CA(Ar)+S_{mixed}) were prepared as reference cases (see Figure S5). Within the shown first three cycles all cells went through a formation process for three discharge-charge cycles at a c-rate of 0.1C. For the sake of comparability, the loading of the active material in all electrodes was kept analogue (0.8 mg cm^{-2}).

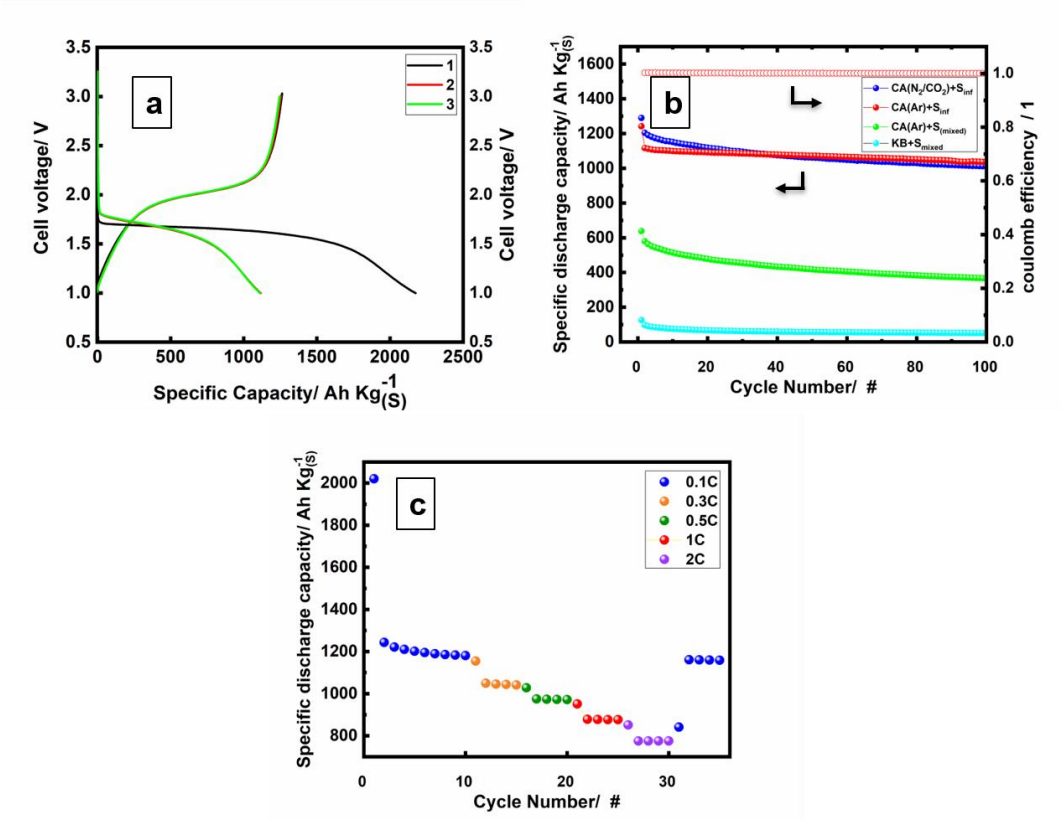

Figure 4 (a) The charge-discharge profile of the formation phases at 0.1C rate for CA(Ar)+$S_{inf.}$ b) Discharge capacity and coulomb efficiency as a function of cycle number at 0.3 C, (c) C-rate depending discharge capacity of CA(Ar)+S_{inf} S electrode in carbonate-based electrolyte.

The voltage–capacity profiles for both CA-based electrodes show solely one voltage plateau at ~1.7 V and 2.0 V for discharge and charge, respectively. The typical redox plateaus at 2.44 and 2.1 V, which are characteristic of the formation of high-order polysulfides (Li_2S_x, $x \geq 4$) and low-order polysulfides (Li_2S_x, $x < 4$), are absent in this case.[43] Several explanations for such a single–plateau reduction and oxidation have been proposed, such as the confinement of short-chain S compounds in the micropores, which triggers the quasi-solid-state reaction mechanism and impedes the polysulfide shuttle effect.[44, 45] Noticeably, most of these reported studies for carbon microporous-based S cathodes showing single-plateau discharge profile are in fact in carbonate-based electrolyte. It was argued by Markevich et al. that the formation of a passivation film on the cathode in contact with the carbonate-based electrolyte is the phenomenon eliminating the polysulfide redox-shuttle.[46] Strikingly, the CA(Ar)+S_{mixed} exhibit a similar one-plateau behavior in the carbonate electrolyte (see Figure 5Sa) while contrarily the KB+S_{mixed} electrodes are not compatible at all with the carbonate electrolyte, failing after first discharge (see Figure 5Sb).

Figure 4b compares the gravimetric discharge capacity of CA+S_{inf}, CA+S_{mixed} and KB+S_{mixed} electrodes. Both CA-based infiltrated cathodes show a higher capacity and superior cyclability than KB+S_{mixed}, confirming the higher S utilization. The higher stability is achieved using CA(Ar) compared to CA(N_2/CO_2) electrodes. Explanation could be given by the fact that all the S in CA(N_2/CO_2) is not fully distributed in micropores. In fact, as mentioned above the S could be found in 0.08 $cm^3\ g^{-1}$ of mesopores, potentially detrimental to the capacity utilization since the electrolyte could still diffuse into the mesopores and dissolve the coordinated S, while such diffusion would be hampered in the case of micropores. The CA(Ar)+S_{mixed} shows a similar cyclability despite the absence of the infiltration process. However, the lower discharge capacity utilization is due to the uncoordinated and surficial S. Nevertheless, the formation of the SEI on the cathode in contact with the carbonate electrolyte would still preserve and trap a certain percentage of the active material (considerably less than the amount of S infiltrated into the micropores) within the carbon matrix, leading to a single-plateau discharge. On the other hand, the failure of the KB+S_{mixed} electrode in the carbonate electrolyte leaves the SEI formation theory puzzling and rectifies the effect of porosity. As long as the application is concerned, the

aerogels show superior rate performance in the carbonate electrolytes, providing a discharge capacity of over 750 Ah kg^{-1}, even at the higher rate of 2C, as shown in Figure 4c. After the subsequent six cycles the capacity stabilizes to a stationary value from about 1200 Ah kg^{-1} to 1170 Ah kg^{-1} at 0.1C. After ten cycles the C-rate is increased to 0.3C. After that the C-rate is doubled every five cycles until 2C is reached, then decreased back to 0.1C. After undergoing various charge–discharge rates, the CA(Ar)+S_{inf} swiftly resumes its capacity of about 1170 A h $kg_{(s)}^{-1}$.

To explore the influence of microporosity compared to the electrolyte type in more details, the identical electrodes were tested in ether-based electrolytes (1M LiTFSI: DOL/DME) in the range 1-3.3V. As depicted in the voltage-capacity profile for CA(Ar)+S_{inf} (Figure 5a), the first cycles in contrast to carbonate-based electrolyte show the two-plateaus behavior elucidating the solution-based rather than the fully quasi-solid-state mechanism. The oxidation of the long-chain polysulfides can be observed in the deeper state of charge. Nevertheless, the impact of the infiltration of the S is rather pronounced compared to the KB+S_{mixed} and CA+S_{mixed} electrodes (see Figure S6a and S6b).

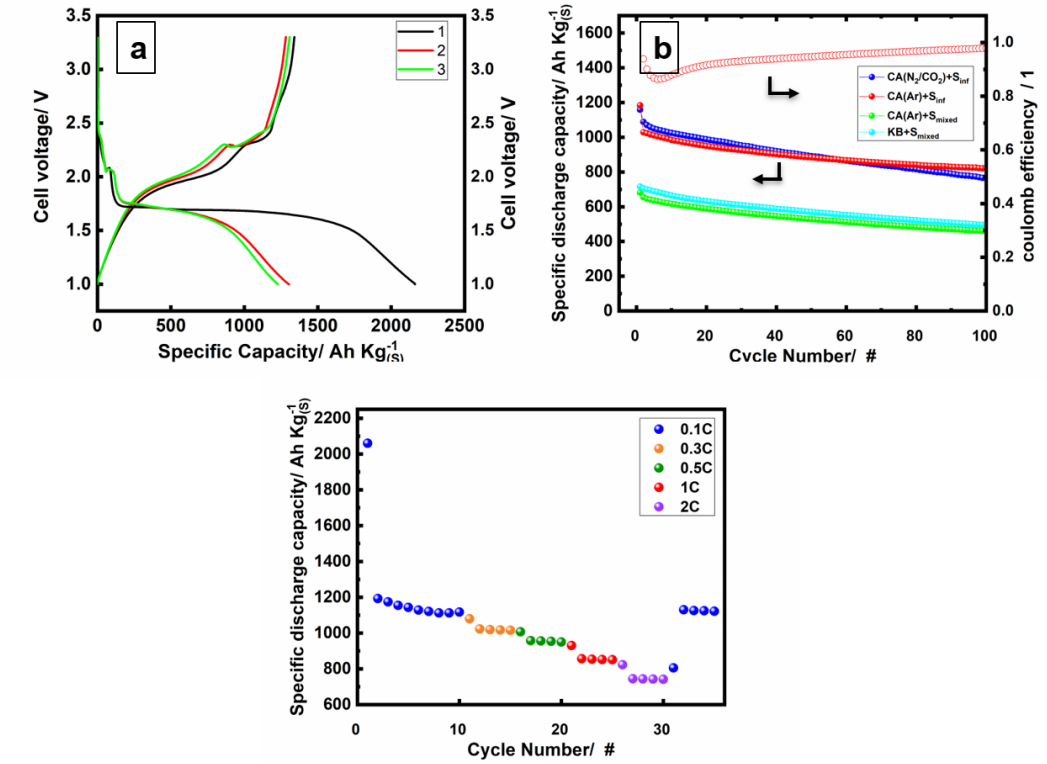

Figure 5(a) The charge-discharge profile of the formation phase at 0.1C rate for 1M LiTFSi: DOL/DME for CA(Ar)+S_{inf} . (b) Discharge capacity and coulomb efficiency as a function of cycle number at 0.3 C. (c) C-rate depending discharge capacity of CA(Ar)+S_{inf} S electrode in ether-based electrolyte.

To investigate and elaborate on the formation and growth of the protection layer on the cathode, electrochemical impedance spectroscopy in symmetrical cathode setup has been implemented. The impedance spectra after 10h of open circuit voltage (OCV) aging have been recorded in carbonate and ether-based electrolyte in contact with the CA(Ar)+$S_{(inf)}$, Figure 6a. Equivalent circuits assigned to the ether electrolyte (Figure 6b, top) is comprised of an electrolyte resistance (R_{el}), inter particle contacts in the composite electrode (R_1Q_1) and the transmission line model for the blocking porous electrode including the electrolyte resistance in the pores (R_{pore}) and a parallel resistance-capacitance element corresponding to the charge transfer (R_2Q_2).[47-50] In the case of the carbonate electrolyte an additional process in mid-frequency region corresponding to the passivation layer on the cathode exposed to the carbonate electrolyte ($R_{film}Q_{film}$) is detected. The contribution of the R_2Q_2 even after full discharge is distinctly noticeable, Figure S7.

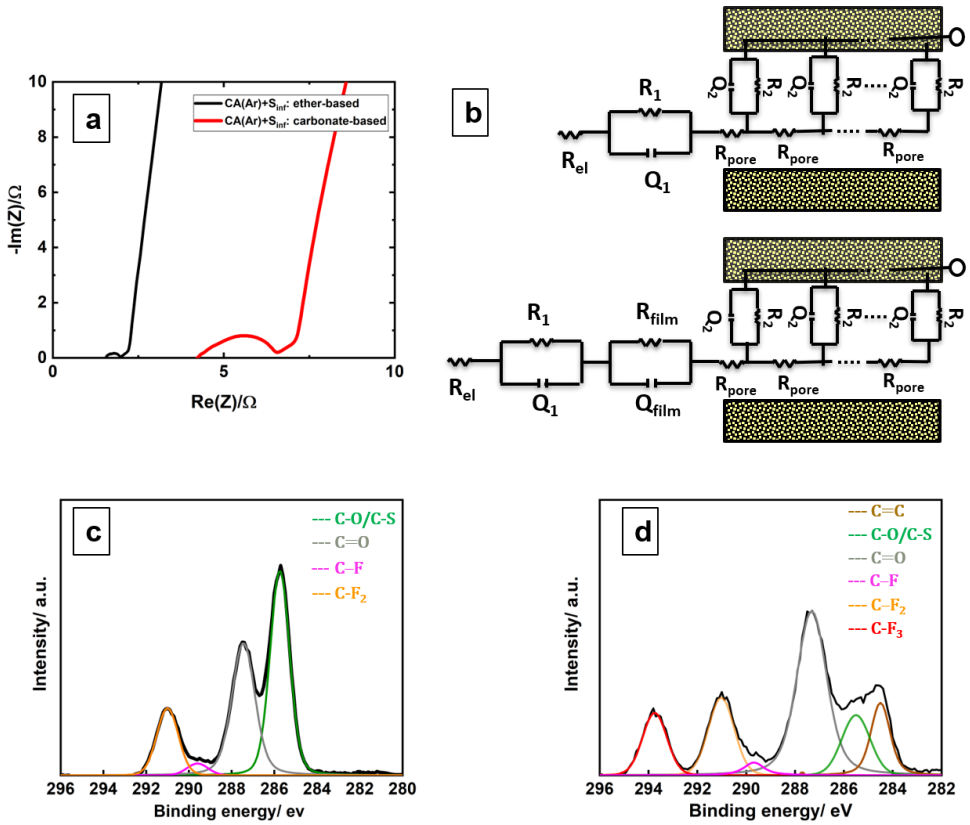

Figure 6 (a) Impedance spectra of symmetrical CA(Ar)+S_{inf} S electrode in carbonate and ether-based electrolyte. (b) Equivalent circuits used for fitting the EIS data for ether (top) and carbonate electrolyte (bottom). (c) C 1s signal of XPS spectra of electrode discharged in carbonate electrolyte. (d) C 1s signal of XPS spectra of electrode discharged in ether electrolyte.

The higher overpotentials observed in the galvanostatic polarization test in carbonate electrolyte in fact comply with the film formation. Interestingly, the C 1S XPS spectra of these cathodes after full discharged, shown in Figure 6 c and d confirm the formation of an additional layer in the carbonate electrolyte. The C=C peak is prominent in the C1s signal of the XPS spectra of the cathode exposed to the ether electrolyte, whereas it disappears entirely in the case of the carbonate electrolyte.

The film formation is thus evidently involved in triggering the quasi-solid-state reaction. On the other hand, as already discussed, the KB+S mixing electrode fails rapidly in the carbonate electrolyte. In the ethereal electrolyte, the trapping of the S in the micropores via the gas-infiltration results in a longer plateau at the lower potentials and hence in a higher discharge capacity. These findings suggest that fully activation of the quasi-solid-state conversion redox at lower potentials requires the encapsulation of the S in the micropores along with the implementation of a film-forming electrolyte, implying that none of these approaches solely would be adequate to suppress polysulfide dissolution and enhance performance in the longer run. It appears that the infiltration technique is mainly responsible for high capacity, while a film forming electrolyte will guarantee its retention and therefore the cyclability of the system.

Finally touching upon the concerns for potential application, the percentage of the active material is of a crucial matter to the achievable energy density. In this context, electrodes with higher loadings, up to the maximum extent the microporosity allows the infiltration of S, were manufactured and investigated (S loading of 1.5 mg cm^{-2}), shown in Figure 7. The discharge capacity profile of the cathode with CA(N_2/CO_2)+S_{inf} indicates a stable cycling behaviour, calling for the design of aerogels with even higher microporosity levels to accommodate further increases in active material. Notably, the mixed CA(Ar)+S_{mixed} electrodes at higher loading of 2.5 mg cm^{-2} despite a noticeable lower capacity values still delivers good cyclability. This is also of relevance for the application, as this system offers energy efficient cathode preparation, relatively high loading of active material, superior cyclability, acceptable capacity after 200 cycles and relatively lower electrolyte amount (20 µL mg^{-1}) in the lab-scale, rendering the system potentially of interest for pouch level investigations. Still, this development can only be regarded as starting point for further optimization of a

promising material class as particularly cathode loading and active material content in the electrode needs to be further increased to facilitate competitive energy density. For the same reason, the performance needs to be demonstrated at more challenging lean electrolyte conditions.

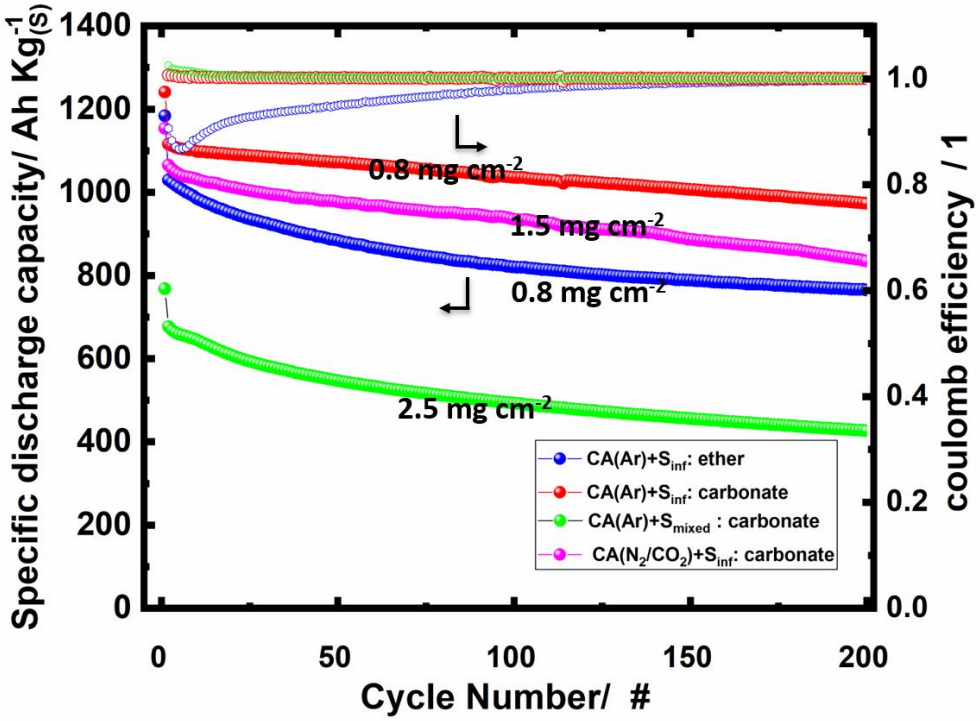

Figure 7 Discharge capacity and coulomb efficiency as a function of cycle number at 0.3 C rate for: CA(Ar)+S_{inf} in ether electrolyte (blue), carbonate electrolyte(red), CA(N_2/CO_2)+S_{inf} with the loading of 1.5 mg cm^{-2} in carbonate electrolyte (purple) and CA(Ar)+S_{mixed} in carbonate electrolyte (green).

Conclusion

In the presented study, a highly porous CA with microporosity up to 0.6 cm^3 g^{-1} as a conductive matrix, incorporating S to serve as the cathode in Li-S batteries is synthesized and investigated. The CA-based cathodes, infiltrated via gas-phase under pressure and high temperature demonstrate a superior discharge capacity of 1000 Ah $kg_{(S)}^{-1}$ for 200 cycles. The combination of S encapsulation in micropores and a film-forming electrolyte, namely a carbonate-based one, has been indicated to fully activate the quasi-solid-state S/Li_2S conversion reaction, suppressing polysulfide shuttle-redox. The aforementioned both phenomena are indeed effective approaches to improve the capacity and the cyclability of the cell, with the latter being more influential and durable. The best performance is achieved in the case of simultaneous implementation of both approaches.

Conflicts of interest

There are no conflicts to declare.

Acknowledgements

The authors thank Dr. Indro Biswas and Dr. Ulrich Hagemann for the XPS experiments and fruitful discussions.

References

1. L. Trahey, F. R. Brushett, N. P. Balsara, G. Ceder, L. Cheng, Y.-M. Chiang, N. T. Hahn, B. J. Ingram, S. D. Minteer, J. S. Moore, K. T. Mueller, L. F. Nazar, K. A. Persson, D. J. Siegel, K. Xu, K. R. Zavadil, V. Srinivasan and G. W. Crabtree, *PNAS*, 2020, **117**, 12550-12557.

2. A. Manthiram, S.-H. Chung and C. Zu, *Adv. Mater.*, 2015, **27**, 1980-2006.
3. Q. Zhang, F. Li, J.-Q. Huang and H. Li, *Adv. Funct. Mater.*, 2018, **28**, 1804589.
4. A. Fotouhi, D. J. Auger, L. O'Neill, T. Cleaver and S. Walus, *Energies*, 2017, **10**, 1937.
5. in *Lithium–Sulfur Batteries*, 2019, DOI: 10.1002/9781119297895.ch12, pp. 293-312.
6. A. Rosenman, E. Markevich, G. Salitra, D. Aurbach, A. Garsuch and F. F. Chesneau, *Adv. Energy Mater.*, 2015, **5**, 1500212.
7. S. Dörfler, H. Althues, P. Härtel, T. Abendroth, B. Schumm and S. Kaskel, *Joule*, 2020, **4**, 539-554.
8. G. Yang, S. Shi, J. Yang and Y. Ma, *J. Mater. Chem. A*, 2015, **3**, 8865-8869.
9. S. Evers and L. F. Nazar, *Acc. Chem. Res.*, 2013, **46**, 1135-1143.
10. T. Li, X. Bai, U. Gulzar, Y.-J. Bai, C. Capiglia, W. Deng, X. Zhou, Z. Liu, Z. Feng and R. Proietti Zaccaria, *Adv. Funct. Mater.*, 2019, **29**, 1901730.
11. in *Lithium–Sulfur Batteries*, 2019, DOI: 10.1002/9781119297895.ch2, pp. 33-69.
12. Z. Li, H. Jiang, N.-C. Lai, T. Zhao and Y.-C. Lu, *Chemistry of Materials*, 2019, **31**, 10186-10196.
13. A. Eftekhari and D.-W. Kim, *J. Mater. Chem. A*, 2020, **8**, 1485-1485.
14. J. Liang, Z.-H. Sun, F. Li and H.-M. Cheng, *Energy Storage Mater.*, 2016, **2**, 76-106.
15. Q. Zhang, X.-b. Cheng, J.-q. Huang, H.-j. Peng and F. Wei, *Carbon*, 2015, **81**, 850.
16. G. Zheng, Y. Yang, J. J. Cha, S. S. Hong and Y. Cui, *Nano Lett.*, 2011, **11**, 4462-4467.
17. R. Yan, M. Oschatz and F. Wu, *Carbon*, 2020, **161**, 162-168.
18. S. Evers and L. F. Nazar, *ChemComm*, 2012, **48**, 1233-1235.
19. E. B. Sebok and R. L. Taylor, in *Encyclopedia of Materials: Science and Technology*, eds. K. H. J. Buschow, R. W. Cahn, M. C. Flemings, B. Ilschner, E. J. Kramer, S. Mahajan and P. Veyssière, Elsevier, Oxford, 2001, DOI: https://doi.org/10.1016/B0-08-043152-6/00173-X, pp. 902-906.
20. S. Xin, L. Gu, N.-H. Zhao, Y.-X. Yin, L.-J. Zhou, Y.-G. Guo and L.-J. Wan, *J. Am. Chem. Soc.*, 2012, **134**, 18510-18513.
21. M. Helen, T. Diemant, S. Schindler, R. J. Behm, M. Danzer, U. Kaiser, M. Fichtner and M. Anji Reddy, *ACS Omega*, 2018, **3**, 11290-11299.
22. J. Gao, M. A. Lowe, Y. Kiya and H. D. Abruña, *J. Phys. Chem. C,*, 2011, **115**, 25132-25137.
23. T. Yim, M.-S. Park, J.-S. Yu, K. J. Kim, K. Y. Im, J.-H. Kim, G. Jeong, Y. N. Jo, S.-G. Woo, K. S. Kang, I. Lee and Y.-J. Kim, *Electrochim. Acta*, 2013, **107**, 454-460.
24. L. Borchardt, M. Oschatz and S. Kaskel, *Chem. Eur. J.*, 2016, **22**, 7324-7351.
25. J. Guo, Y. Xu and C. Wang, *Nano Lett.*, 2011, **11**, 4288-4294.
26. F.-f. Zhang, X.-b. Zhang, Y.-h. Dong and L.-m. Wang, *J. Mater. Chem*, 2012, **22**, 11452-11454.
27. J. T. Lee, Y. Zhao, S. Thieme, H. Kim, M. Oschatz, L. Borchardt, A. Magasinski, W.-I. Cho, S. Kaskel and G. Yushin, *Adv. Mater.*, 2013, **25**, 4573-4579.
28. Y. Xu, Y. Wen, Y. Zhu, K. Gaskell, K. A. Cychosz, B. Eichhorn, K. Xu and C. Wang, *Adv. Funct. Mater.*, 2015, **25**, 4312-4320.
29. R. W. Pekala, J. C. Farmer, C. T. Alviso, T. D. Tran, S. T. Mayer, J. M. Miller and B. Dunn, *J Non Cryst Solids*, 1998, **225**, 74-80.
30. *Aerogels Handbook*, 2011.
31. Z. Li, X. Li, Y. Liao, X. Li and W. Li, *J. Power Sources*, 2016, **334**, 23-30.
32. Z. Fang, Y. Luo, H. Wu, L. Yan, F. Zhao, Q. Li, S. Fan and J. Wang, *Carbon*, 2020, **166**, 183-192.
33. C. Yang, P. Li, J. Yu, L.-D. Zhao and L. Kong, *Energy*, 2020, **201**, 117718.
34. M. Schwan and L. Ratke, *Carbon*, 2016, **2**, 12.
35. 2020.
36. A. M. Saeed, P. M. Rewatkar, H. Majedi Far, T. Taghvaee, S. Donthula, C. Mandal, C. Sotiriou-Leventis and N. Leventis, *ACS Appl. Mater. Interfaces*, 2017, **9**, 13520-13536.
37. C. Lin and J. A. Ritter, *Carbon*, 2000, **38**, 849-861.
38. A. C. Ferrari and J. Robertson, *Phys. Rev. B*, 2000, **61**, 14095-14107.
39. J. Robertson, *Adv. Phys*, 1986, **35**, 317-374.
40. X. Lu, O. Nilsson, J. Fricke and R. W. Pekala, *J. Appl. Phys*, 1993, **73**, 581-584.
41. B. Meyer, *Chem. Rev.*, 1976, **76**, 367-388.
42. G. Zhou, L.-C. Yin, D.-W. Wang, L. Li, S. Pei, I. R. Gentle, F. Li and H.-M. Cheng, *ACS Nano*, 2013, **7**, 5367-5375.
43. C. Barchasz, F. Molton, C. Duboc, J.-C. Leprêtre, S. Patoux and F. Alloin, *Anal. Chem*, 2012, **84**, 3973-3980.
44. M. Helen, M. A. Reddy, T. Diemant, U. Golla-Schindler, R. J. Behm, U. Kaiser and M. Fichtner, *Sci. Rep.*, 2015, **5**, 12146.

45. Z. Peng, W. Fang, H. Zhao, J. Fang, H. Cheng, T. N. L. Doan, J. Xu and P. Chen, *J. Power Sources*, 2015, **282**, 70-78.
46. E. Markevich, G. Salitra, A. Rosenman, Y. Talyosef, F. Chesneau and D. Aurbach, *Electrochem. commun.*, 2015, **60**, 42-46.
47. M. Adamič, S. D. Talian, A. R. Sinigoj, I. Humar, J. Moškon and M. Gaberšček, *(J. Electrochem. Soc.*, 2018, **166**, A5045-A5053.
48. N. A. Cañas, K. Hirose, B. Pascucci, N. Wagner, K. A. Friedrich and R. Hiesgen, *Electrochim. Acta*, 2013, **97**, 42-51.
49. Z. Deng, Z. Zhang, Y. Lai, J. Liu, J. Li and Y. Liu, *J. Electrochem. Soc.*, 2013, **160**, A553-A558.
50. J. Häcker, C. Danner, B. Sievert, I. Biswas, Z. Zhao-Karger, N. Wagner and K. A. Friedrich, *Electrochim. Acta*, 2020, **338**, 135787.